



Citation for published version:

Chartier, A, Forte, B, Deshpande, K, Bust, GS & Mitchell, C 2016, 'Threedimensional modeling of highlatitude scintillation observations', *Radio Science*, vol. 51, no. 7. <https://doi.org/10.1002/2015RS005889>

DOI:

[10.1002/2015RS005889](https://doi.org/10.1002/2015RS005889)

Publication date:

2016

Document Version

Peer reviewed version

[Link to publication](#)

This is the peer reviewed version of the following article: Alex Chartier Biagio Forte Kshitija Deshpande Gary Bust Cathryn Mitchell (2016) Threedimensional modeling of highlatitude scintillation observations. *Radio Science*, 51(7), which has been published in final form at [10.1002/2015RS005889](https://doi.org/10.1002/2015RS005889). This article may be used for non-commercial purposes in accordance with Wiley Terms and Conditions for Self-Archiving.

University of Bath

General rights

Copyright and moral rights for the publications made accessible in the public portal are retained by the authors and/or other copyright owners and it is a condition of accessing publications that users recognise and abide by the legal requirements associated with these rights.

Take down policy

If you believe that this document breaches copyright please contact us providing details, and we will remove access to the work immediately and investigate your claim.

1 **Three-Dimensional Modeling of High-Latitude Scintillation Observations**

2

3 ¹ Alex Chartier, ² Biagio Forte, ³ Kshitija Deshpande, ¹ Gary Bust, ² Cathryn Mitchell

4

5 ¹ Johns Hopkins University Applied Physics Laboratory, 11100 Johns Hopkins Road,
6 Laurel MD 20723

7 ² Dept. Electronic and Electrical Engineering, University of Bath, Claverton, Bath, UK

8 ³ Bradley Department of Electrical and Computer Engineering, Virginia Tech, 1901
9 Innovation Dr., Blacksburg, VA 24061

10

11

12 **Key Points**

13

14 1. Modeled fractional electron density fluctuations must vary to match GPS
15 observations

16 2. Ensemble, multiple phase screen 3D scintillation model developed

17 3. Reasonable match achieved between modeled and observed signals

18

19 **Abstract**

20

21 Global Navigation Satellite System (GNSS) signals exhibit rapid fluctuations at high
22 and low latitudes as a consequence of propagation through drifting ionospheric
23 irregularities. We focus on the high latitude scintillation problem, taking advantage
24 of a conjunction of EISCAT Incoherent Scatter Radar (ISR) observations and a GPS
25 scintillation monitor viewing the same line-of-sight. Just after 20:00 UT on 17
26 October 2013, an auroral E-region ionization enhancement occurred with
27 associated phase scintillations. This investigation uses the scintillation observations
28 to estimate the ionospheric electron density distribution beyond the spatial
29 resolution of the ISR (5 - 15 km along the line-of-sight in this case). Following the
30 approach of *Deshpande et al.* [2014], signal propagation is modeled through a
31 specified density distribution. A multiple phase screen propagation algorithm is
32 applied to irregularities conforming to the description of *Costa and Kelley* [1977]
33 and constrained to match the macroscopic conditions observed by the ISR. A 50-
34 member ensemble of modeled outputs is approximately consistent with the
35 observations according to the standard deviation of the phase (σ_p). The observations
36 have $\sigma_p = 0.23$ radians, while the ensemble of modeled realizations has $\sigma_p = 0.23$
37 $+0.04 -0.04$. By comparison of the model output with the scintillation observations,
38 we show that the density fluctuations cannot be a constant fraction of the mean
39 density. The model indicates that E-region density fluctuations whose standard
40 deviation varies temporally between 5 - 25% of the mean (ISR-observed) density
41 are required to explain the observed phase scintillations.

42 **1. Introduction**

43

44 Scintillation is the phenomenon of random phase and intensity fluctuations in
45 received radio signals. Scintillation is seen in transionospheric signals in the
46 frequency range of 100 MHz – 4 GHz [Basu *et al.*, 1988; Aarons & Basu, 1994]. At
47 high latitudes, scintillation caused by E-region auroral events can be strong enough
48 to cause loss of lock by GPS L-band receivers [Skone and De Jong, 2000; Smith *et al.*,
49 2008]. Physically, scintillation is caused by diffractive scattering and refractive
50 lensing of signals by ionospheric electron density structures. At GPS frequencies
51 (L1: 1575 MHz, L2: 1228 MHz), intermediate-scale irregularities (approximately
52 0.1-10 km) are responsible for diffractive scattering.

53

54 1.1 Signal propagation

55 At high latitudes, phase scintillation is frequently observed without accompanying
56 intensity scintillation [Aarons, 1997; Skone *et al.*, 2008; Azeem *et al.*, 2013]. The
57 phenomenon has been addressed theoretically by Booker *et al.* [1950], Rino [1979],
58 Yeh and Liu [1982], Kintner *et al.* [2007] and others. Signal phase and intensity can
59 behave differently because they respond to different irregularity scale sizes. The
60 Fresnel radius defines the most effective irregularity scale for intensity scintillation.
61 The Fresnel radius is ~ 270 m for L1 signals when the irregularity layer is at a range
62 of 150 km from the receiver. In principle, the signal phase responds to irregularities
63 of all scale sizes. In practice, however, an artificial outer scale is imposed beyond
64 which electron density variations have practically no effect [Forte and Radicella,

65 2004]. This outer scale occurs because observational data are detrended to remove
66 long period fluctuations. In the case of a 0.1 Hz filter and a 300 m/s effective velocity
67 there is an artificial outer scale of 3000 m for the phase.

68

69 1.2 Auroral scintillation

70 Evidence of scintillation on L-band GPS signals in conjunction with auroral
71 structures has been provided by *Skone et al.* [2001], *Prikryl et al.* [2011] and *Kinrade*
72 *et al.* [2013]. Currently there are no E-region electron density observations of
73 sufficiently high spatial resolution to determine the irregularity distributions
74 responsible for these scintillations.

75

76 The aim of this investigation is to determine the irregularity distribution
77 characteristics using a constrained modeling approach to match the scintillation
78 observations. Despite the unprecedented conjunction of data available in this case,
79 some model parameters remain unconstrained by observations. These are the
80 effective irregularity drift velocity, the fractional density fluctuation ($\Delta N/N$) and the
81 axial ratio of the irregularities. Choices of these parameters are informed by the
82 parameter space search performed by *Deshpande et al.* [2014], by prior
83 observational studies and by the observed scintillation signal.

84

85

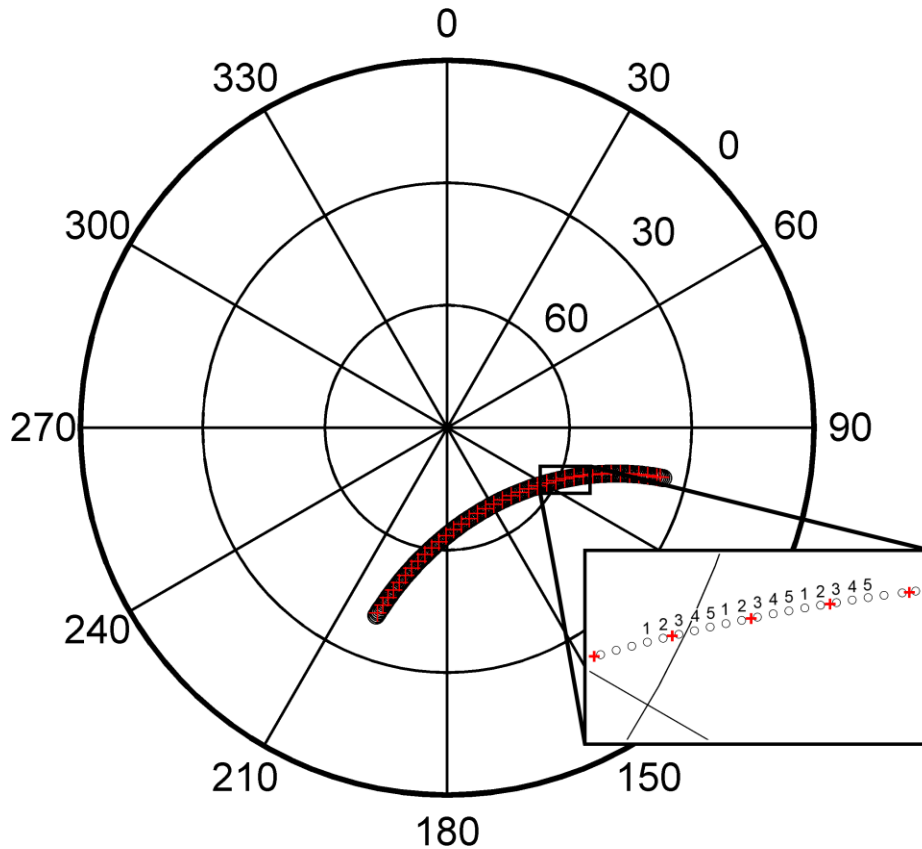
86 **2. Observations**

87

88 The present study is based on an experiment where the European Incoherent
89 Scatter Radar (EISCAT) is operated along the line of sight of GPS satellites, by
90 tracking their motion across the sky. In the selected case study phase scintillation is
91 observed at Tromsø, Norway just after 20:00 UT on 17 October 2013. The K_p index
92 of 1+ between 18:00-21:00 UT indicates quiet geomagnetic conditions during the
93 experiment. Similar scintillation cases are not especially rare in themselves, but we
94 are not aware of another case with direct supporting observations from EISCAT
95 along the GPS line of sight.

96

97 The EISCAT UHF antenna tracked the location of GPS satellite PRN 23, making
98 ionospheric electron density observations along the line-of-sight using the
99 calibrated backscattered power from its 931 MHz transmissions. The dish changed
100 position every 5 minutes, with the satellite moving across it in that period. Five 60-
101 second integrations are made at each location, from which electron density, ion and
102 electron temperature and beam-parallel ion drifts can be calculated. This EISCAT
103 experiment was monostatic, so no estimate of cross-track drifts can be made. At the
104 time of interest (\sim 20:05 UT), the angle between the beam and the magnetic field is
105 around 25°. The azimuth and elevation of the beam are shown in Figure 1.



106

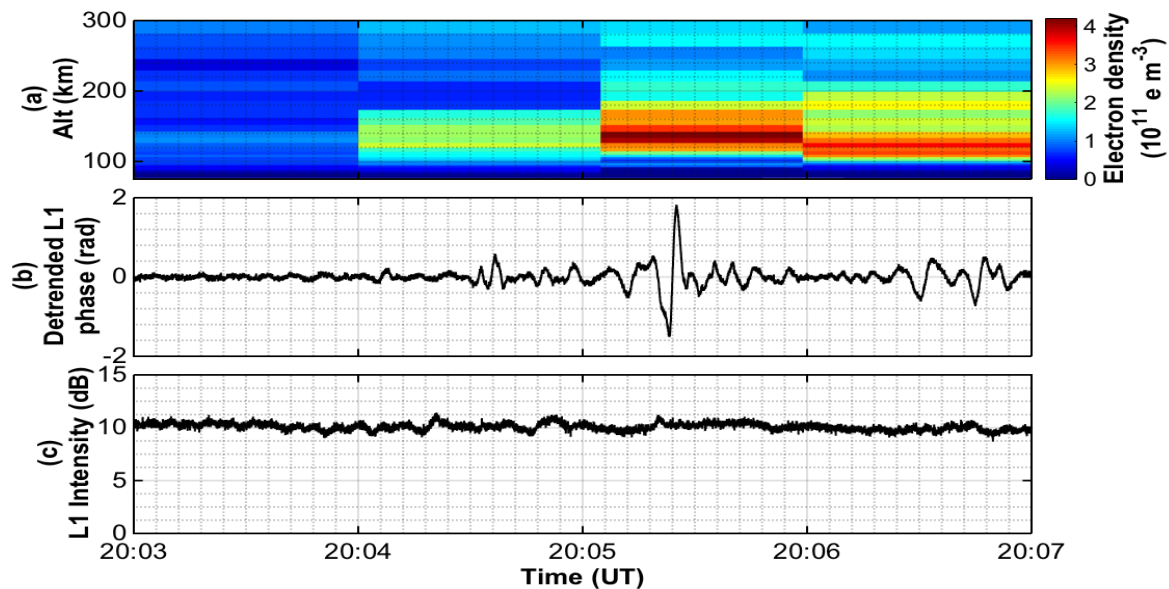
107 *Figure 1: The azimuth and elevation of the EISCAT beam during the scintillation*
 108 *experiment. The beam moves every five minutes, stopping at the central location of the*
 109 *GPS satellite for that period.*

110

111 A collocated Novatel GSV4004 GPS ionospheric scintillation monitor receives
 112 transmissions from the same satellite (PRN 23). The scintillation monitor outputs
 113 scintillation indices, TEC and TEC rate-of-change at one-minute intervals, together
 114 with 50 Hz signal intensity and phase [Van Dierendonck et al., 1993]. The 50 Hz
 115 intensity and phase are used for this study.

116

117 EISCAT electron densities and GPS scintillation observations are shown in Figure 2.
118 Scintillation data are detrended using a third-order polynomial followed by a sixth-
119 order 0.1 Hz high-pass Butterworth filter. At 20:05:20 UT, a phase scintillation spike
120 of over 3 radians peak-to-peak is observed that corresponds with enhanced E-
121 region electron densities that peak at 4.17×10^{11} electrons/m³ at 132 km. Smaller
122 phase scintillations occur from 20:04:30 to 20:07:00 UT. No corresponding spike in
123 the observed signal intensity is observed above the noise floor.



124

125 *Figure 2: (a) EISCAT electron densities, (b) 50 Hz detrended GPS L1 carrier phase, (c)*

126

50 Hz signal intensity

127

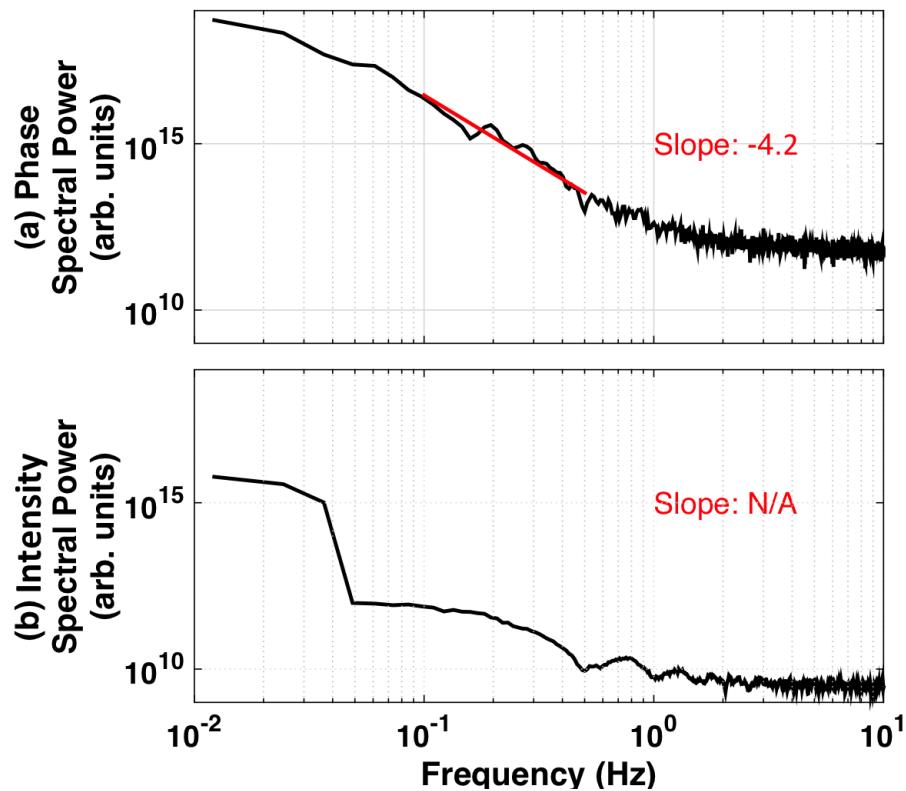
128 Power spectral densities are calculated on the unfiltered signal phase and intensity

129 during the same period to determine the characteristics of the ionospheric

130 irregularities responsible for the scintillation. The region > 0.1 Hz is directly

131 comparable with the filtered signal of Figure 2. Welch's power spectral density

132 method is used with a Hamming window, eight segments and a 50% overlap. The
133 time interval considered is 20:03 to 20:07 UT. These spectra are shown in Figure 3.
134 The signal phase has a clear linear slope of -4.2 down to a noise floor above 1 Hz.
135 The signal power does not have a single clear slope, although an increase above the
136 noise floor is evident at lower frequencies.



137
138 *Figure 3: Power spectral density of (a) GPS signal phase and (b) signal intensity. A*
139 *linear fit of -4.2 is achieved to the phase spectrum unaffected by noise (defined as*
140 *between 0.1 - 0.5 Hz). No linear slope can be identified in the intensity.*

141

142

143 **3. Modeling**

144

145 Given the supporting information available from EISCAT, it is possible to model GPS
146 signal propagation through the ionosphere in this case. The comparison between
147 modeled and observed results is used to understand what combination of
148 parameters drives this particular event. The SIGMA scintillation model developed by
149 *Deshpande et al.* [2014] is used here. SIGMA is a three-dimensional, multiple phase
150 screen scintillation model that accounts for satellite and irregularity motion, and
151 allows for anisotropic irregularity modeling. For this study, EISCAT electron density
152 data are ingested to specify the macro-scale ionospheric electron densities. The
153 geometry of the electron density representation is modified from the approach of
154 *Deshpande et al.* [2014], but the signal propagation algorithm and the irregularity
155 spectrum generator (based on the formulation of *Costa and Kelley*, [1977]) remain
156 unchanged. The spectrum \mathbf{P} , shown in Equation 1, depicts a Gaussian density
157 distribution along the magnetic field direction k_z and a power law variation
158 perpendicular to it (in the plane of k_x and k_y):

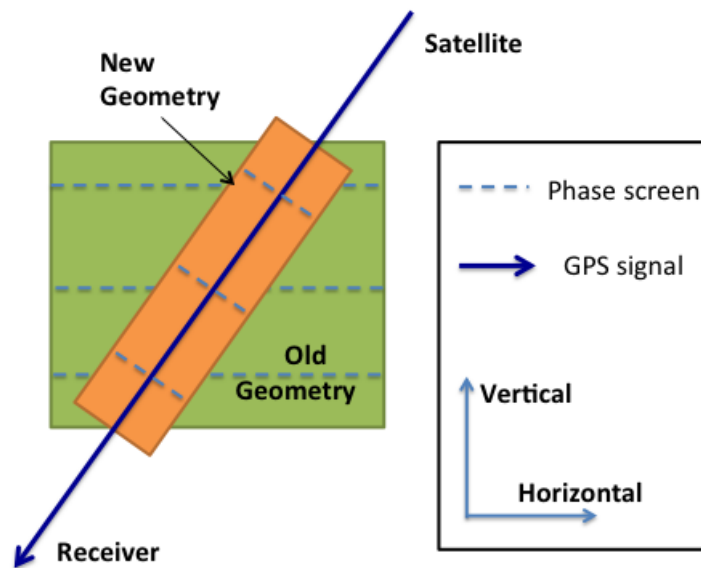
159
$$\mathbf{P}(\mathbf{k}) = \frac{a \gamma \sin(3\pi/\gamma)}{4\pi^2 k_0^3} \Delta N^2 \cdot \left\{ \left(1 + \frac{k_x^2 + k_y^2 + a^2 k_z^2}{k_0^2} \right)^{-\gamma/2} \right\}^{-1} \quad (1)$$

160 Here $\mathbf{k} = (k_x, k_y, k_z)$ is the spatial wave number vector, γ is the spectral index, a is
161 the axial ratio, ΔN is the root-mean-square density fluctuation and k_0 is the
162 wavenumber associated with the outer scale of the irregularity spectrum.

163

164 3.1 Electron density representation

165 A geometry change is introduced to SIGMA for this study in order to drastically
166 reduce computation times. Instead of using a static horizontal/vertical grid large
167 enough to capture all ray paths throughout the experiment, we align our grid along
168 the satellite-receiver line of sight at each timestep (see Figure 4). The result is that
169 the representation volume must only extend a few Fresnel radii in the
170 perpendicular directions to capture weak scatter effects, and so computation times
171 are reduced down to faster than real-time for short (five-minute) simulation periods
172 (depending on resolution). This approximation is valid only in weak scatter cases,
173 such as the case addressed here. A larger perpendicular extent would be required to
174 capture the effects of strong scatter.
175



176
177 *Figure 4: The geometry change introduced to SIGMA for this study. The new geometry*
178 *(orange) allows for smaller phase screens and thus faster computation times and*
179 *lower memory requirements.*

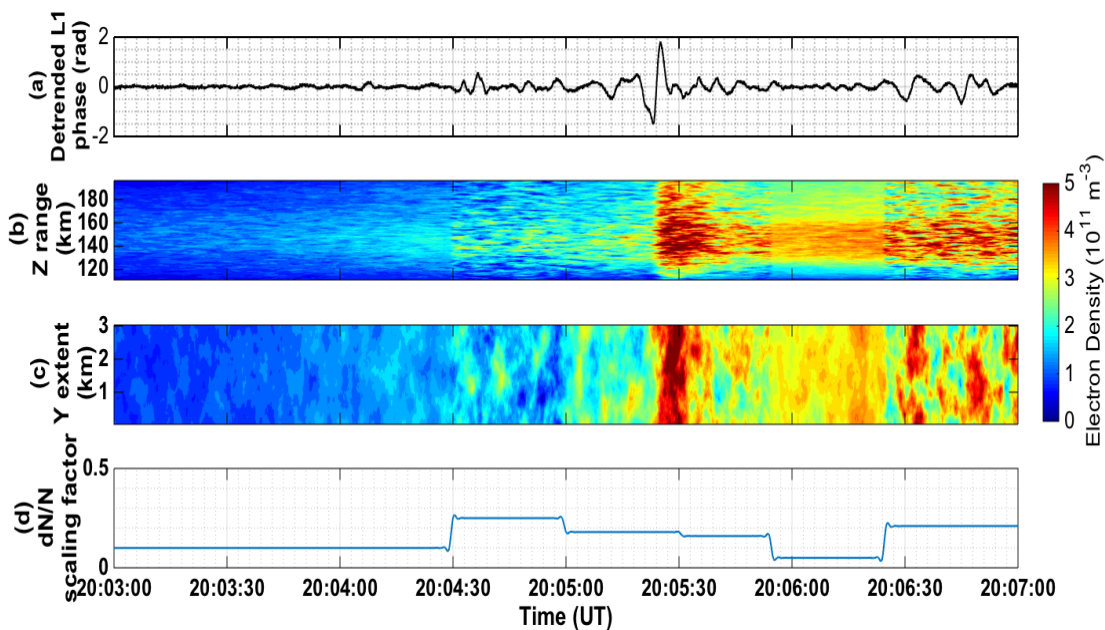
180

181 To understand the scintillation that results from signal propagation through a given
182 ionospheric irregularity distribution, the altitude and thickness of the irregularity
183 layer and the apparent velocity perpendicular to the line-of-sight must be known.
184 We do not have direct observations of these parameters, so it is necessary to make
185 some assumptions. Given the electron density enhancements observed by EISCAT
186 and shown in Figure 2, we assume associated irregularities are formed in the region
187 ~95 – 175 km altitude (110 – 200 km range). The gradients associated with the
188 irregularities (ΔN) are assumed to be a varying proportion of the background
189 density, so that the mean-squared fractional fluctuation density $\overline{\left(\frac{\Delta N}{N}\right)^2}$ is allowed to
190 vary in time. In this case EISCAT is operated in mono-static mode and so observes
191 only the component of bulk plasma velocity in a single line-of-sight between the GPS
192 satellite and receiver, so it is not possible to deduce the effective drift velocity of the
193 irregularities. A velocity of 300 m/s is found to be the lowest that produces an
194 accurate match to both the phase and intensity spectra shown in Figure 3. This is
195 below the ion acoustic velocity (~500 m/s at 150 km altitude increasing to ~1000
196 m/s at 220 km, using EISCAT temperatures and assuming ion molar mass of 28) and
197 well within the normal range of ion drift velocities seen at auroral latitudes, which
198 can be as high as 1000 m/s or more [e.g. *Chisham et al., 2007*]. The slope of the
199 power spectral density is set to -4.2 and there is effectively no outer scale (lengths
200 beyond 3 km are removed by the 0.1 Hz high pass filter). The axial ratio is set to 1 in
201 this case. This is necessary because, in this case, values larger than 1 cause the
202 modeled intensity fluctuations to rise above what is observed. It is worth noting that

203 this value is much lower than what *Gola et al.* [1992] found to fit most auroral cases
204 (values between 6 – 15), so this event may be seen as unusual.

205

206 It is not possible to match the time-domain phase signal (Figure 2) with $\overline{\left(\frac{\Delta N}{N}\right)^2}$ set to
207 a constant, so it is necessary to vary ΔN between 5 – 25 % of N . Even with this, the
208 large (> 3 radian) spike observed at 20:05:25 cannot be reproduced, so a kilometer-
209 scale enhancement is added to the irregularity spectrum at that time. This transient
210 spike has no appreciable effect on the modeled spectra. The resulting modeled
211 electron density distribution is shown in Figure 5.



212

213 *Figure 5: (a) the observed detrended phase is repeated from Figure 2, (b) range-time*
214 *profile of an example model electron density configuration, based on EISCAT*
215 *observations of the background density with one realization of Costa-Kelley*
216 *irregularities added (c) cross-track profile of the same model densities, and (d) the*

217 *variable irregularity scaling factor. Three phase screens are constructed*
218 *perpendicular to Z (at 125-, 155- and 185-km) from this density distribution.*

219

220 The electron density representation shown in Figure 5 is moved along the Y-
221 direction, across the direction of signal propagation (Z), at an effective drift velocity
222 of 300 m/s. This is the lowest velocity that could be used that matched the observed
223 phase scintillation without changing parameters that would enhance the modeled
224 signal intensity above what was observed. A sliding box is applied so that the X
225 extent is always 3000 m (equivalent to 0.1 Hz at 300 m/s effective drift velocity),
226 the same as the Y extent. A larger X/Y extent would have no effect on the result
227 because a 0.1 Hz high pass filter is applied to the results (described below).

228

229 3.2 Signal propagation

230 The signal propagation algorithm developed by *Deshpande et al.* [2014] remains
231 unchanged here. This is a modified version of *Rino's* [1979] algorithm, so the
232 electron density distribution in a layer is used to calculate a phase screen that is
233 applied to the signal. Following *Knepp* [1983], multiple phase screens (three in this
234 case) are used so that re-scattering of the signal can be modeled. This is potentially
235 an important feature at high latitudes where the irregularity region can extend for
236 tens of kilometers or more due to the near-vertical orientation of the magnetic field.

237

238 The model configuration used for these simulations is set out in Table 1.

239

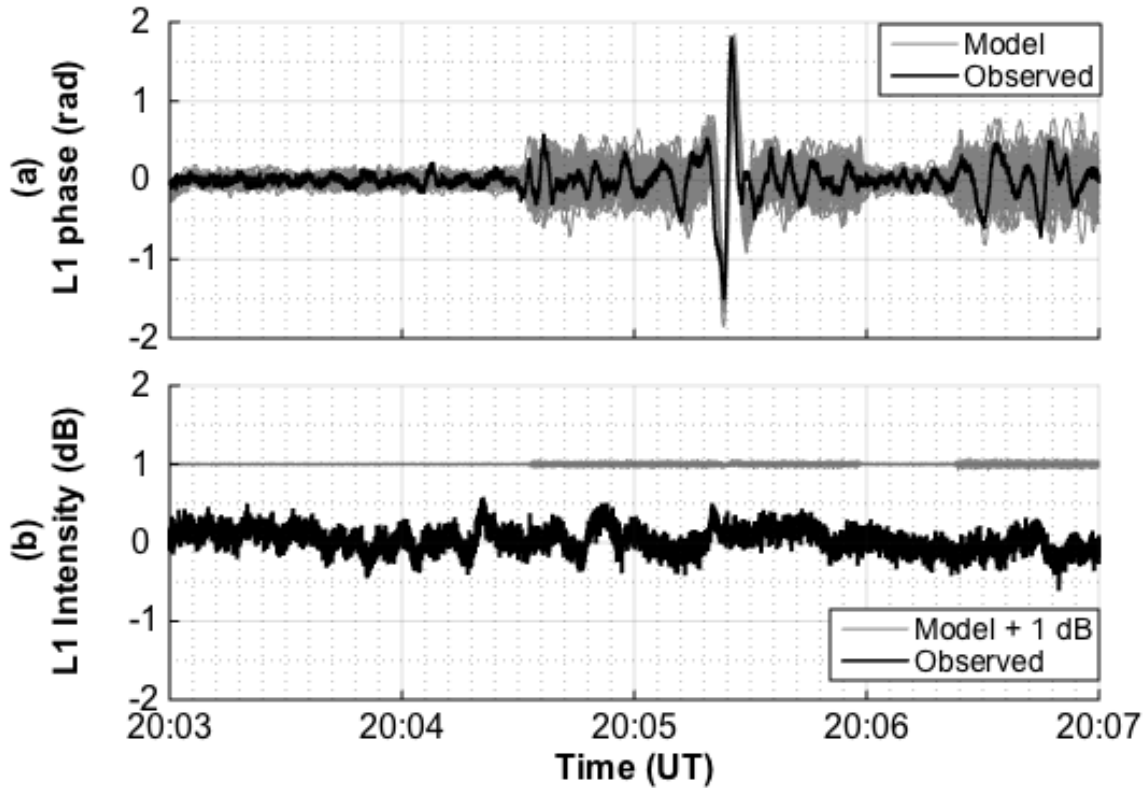
240 **Table 1: Model configuration**

Parameter	Value
Sample frequency	10 Hz
Effective drift velocity	300 m/s
High-pass filter cutoff	0.1 Hz
Outer scale	3000 m (effectively none)
Axial ratio	1
Spectral index	4.2
Phase screens	3 (at 125-, 155- and 185-km range)
Resolution (X, Y, Z)	30, 30, 100 m
Grid size (X, Y, Z)	3000, 3000, 90 000 m

241

242 Fifty realizations of the model are produced using this configuration with different
 243 random number seeds for the irregularities. Figure 6 shows that the model
 244 reproduces the major features of the observed phase scintillation pattern in the time
 245 domain. Low-level (<0.25 radians peak-to-peak) phase fluctuations are observed
 246 before 20:04:30. Fluctuations increase to a moderate level (~1 radian peak-to-peak)
 247 between 20:04:30 and 20:05:55, with a large (>3 radians peak-to-peak) spike at
 248 about 20:05:25. There is a second low-level phase between 20:05:55 and 20:06:20,
 249 followed by a slightly more intense period (~1.5 radians peak-to-peak) thereafter.
 250 Both the modeled and the observed intensity fluctuations are small at all times.
 251 Slight enhancements seen in the modeled intensity fluctuations appear to be within

252 the receiver noise of the observed intensity fluctuations (model values are shifted
253 up 1 dB so they can be seen clearly).



254

255 *Figure 6: (a) the modeled (50 realizations in grey) and observed (bold black)*
256 *detrended L1 carrier phase and (b) the L1 intensity. The modeled intensity is shifted up*
257 *1 dB so that it can be seen clearly.*

258

259 The standard deviation is used to provide a quantitative performance metric here.

260 This is calculated as shown in Equation 2:

261
$$\sigma_p = \sqrt{\langle \varphi^2 \rangle - \langle \varphi \rangle^2} \quad (2)$$

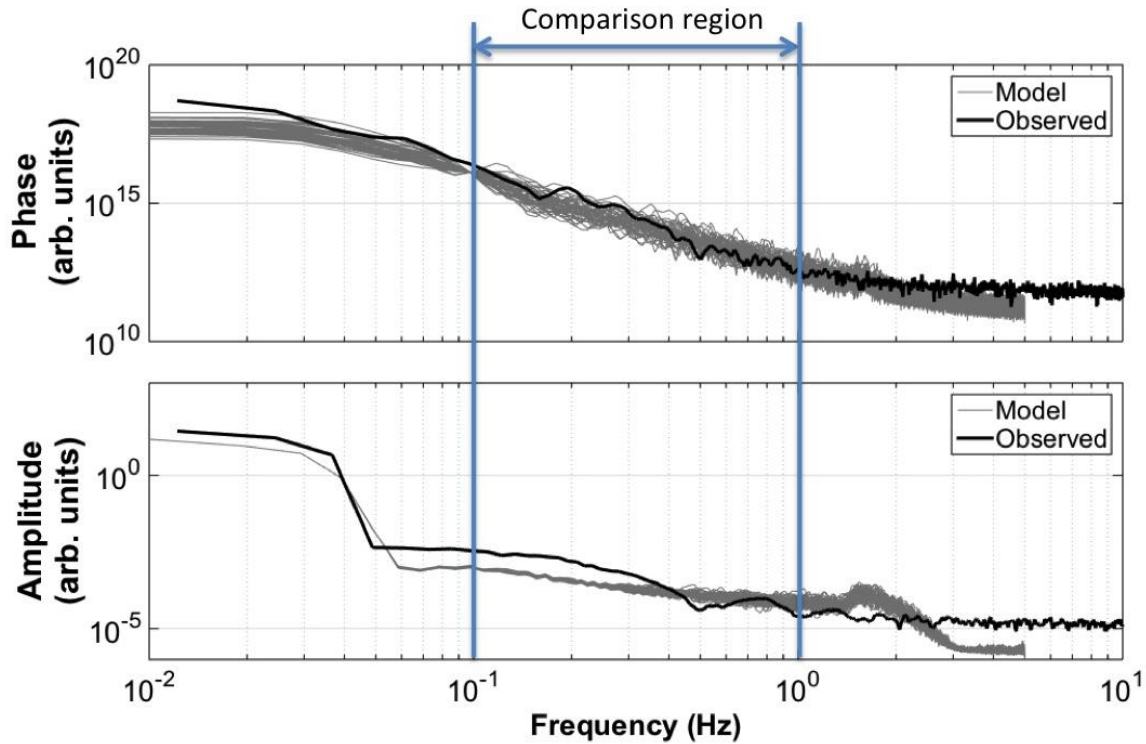
262 where φ is the detrended L1 carrier phase in radians and means are calculated over

263 the time-series shown in Figure 6. The observations have $\sigma_p = 0.23$ radians, while

264 the ensemble of modeled realizations has $\sigma_p = 0.23 +0.04 -0.04$ radians (using mean,
265 maximum and minimum model values). It is worth noting that a single phase screen
266 approach captures less scattering than the multiple phase screen approach in this
267 case. The same model configuration as used above, except with a single screen at
268 155-km, produces lower $\sigma_p = 0.19 +0.03 -0.04$ radians.

269

270 The Power Spectral Density (PSD) of the modeled phase and intensity are compared
271 against the observations in Figure 7. The results are directly comparable in the
272 range $10^{-1} - 10^0$ Hz, where the signals are both above the noise floor and below the
273 artificial 3000 m (equivalent to 0.1 Hz at 300 m/s effective drift velocity) outer scale
274 imposed on the model for reasons of computational efficiency. In that range, the
275 modeled and observed phase signals are in agreement since the observations lie
276 within the range of model realizations. The modeled and observed power are both
277 extremely weak and, while there is not a uniform slope evident in the observations,
278 the two datasets can be considered approximately consistent. The observed
279 intensity PSD has a similar shape at times outside of the phase scintillation event, so
280 the two effects are likely unrelated.



281

282 *Figure 7: Power spectral densities of (a) phase and (b) intensity from the observations*
 283 *and 50 realizations of the model between 20:03 and 20:07 UT. Model values are*
 284 *normalized at 0.1 Hz.*

285

286 **4. Discussion**

287

288 A new technique has been developed to ingest electron density observations into
 289 the SIGMA scintillation model. This development, combined with a geometry change
 290 that dramatically reduces computation times, allows for ensemble modeling of
 291 ionospheric scintillation. These developments have been used to compare model
 292 results against real scintillation observations in a specific auroral case study, and to
 293 determine likely characteristics of the ionospheric irregularities responsible.

294

295 In this case, the model-observation comparison makes it possible to test the
296 assumption that the mean-squared fractional density of ionospheric irregularities
297 responsible for scintillation is a constant. Thanks to the availability of co-aligned
298 EISCAT and GPS data, it is possible to show that this assumption does not hold in
299 this case. The magnitude of the phase scintillations is clearly not proportional to the
300 background density as observed by EISCAT. In the model, the fraction $\frac{\Delta N}{N}$ has to be
301 adjusted between 5-25% to achieve a match to the observations. A similar match
302 could not have been achieved through adjustment of the other free parameters
303 (effective drift velocity, axial ratio) within reasonable physical limits. This case may
304 well be unusual since these irregularities are caused by an auroral E-region
305 enhancement rather than by F-region convective processes. The unusual nature of
306 this event is underlined by the steep slope of the phase PSD (-4.2).

307

308 It is possible to assess the performance of SIGMA in reproducing the observations if
309 two limitations are taken into account. These are that an observational noise floor is
310 evident above ~ 1 Hz, and that the model is applied to scales < 3000 m (frequencies
311 higher than 0.1 Hz). Within the region where a direct comparison can be made (0.1 –
312 1 Hz), the results support the conclusion that the formulation of *Costa & Kelley*
313 [1977] provides an accurate description of these irregularities, and that our
314 multiple phase screen signal propagation algorithm is suitable to characterize signal
315 propagation in this case. It is worth noting that the transverse velocity of the
316 irregularities (300 m/s) had to be estimated because of a lack of supporting

317 observational evidence. The lowest suitable velocity was chosen here – a lower
318 velocity would have required an increase in ΔN that would have caused more
319 intensity scintillation than was observed. The axial ratio also had to be set to a
320 rather unusual value of 1 in order to prevent any increase in the modeled intensity
321 scintillation above what was observed.

322

323 The ‘frozen-in’ assumption was used in the model results presented here. Since the
324 model is broadly consistent with the observations, it appears there is no need to
325 invoke a more complicated, time-evolving irregularity distribution in this case.

326 However our results do not exclude the possibility that the irregularities evolve in
327 time. The current modeling approach could be adapted to deal with time-evolving
328 irregularities if cases are identified that cannot be represented otherwise.

329

330 The development of SIGMA for this study has greatly reduced computation times
331 down to approximately real-time for simulation periods of a few minutes (running
332 in Matlab on a laptop computer). This development permits the use of grids with Z-
333 extent large enough to simulate the effects of multiple scatter, which may be
334 important for high-latitude scintillation. In this case we noted a discrepancy
335 between the model using three phase screens and using just one. Assuming that the
336 irregularity region truly extends for 90 km in the Z-direction, as was specified here,
337 this finding indicates that the effects of multiple scatter should be taken into
338 account. While the observed density enhancement extends for 90 km, there is no

339 proof that irregularities extend throughout that region. Therefore we cannot
340 exclude that a more intense but narrower region of irregularities exists.

341

342

343 **5. Conclusions**

344

345 The SIGMA model has reasonably accurately reproduced scintillations observed at
346 Tromsø, which indicates that the modeled ionospheric irregularity distribution and
347 signal propagation algorithm are likely to be consistent with the observations. A
348 new grid geometry has been applied to the SIGMA model to achieve these results,
349 with the positive consequence that computation times are greatly reduced. In this
350 case, the results show that $\frac{\Delta N}{N}$ is not a constant, but the frozen-in assumption is
351 consistent with the observations. Coupled with the steep slope of the phase PSD (-
352 4.2) and axial ratio of 1, effective drift velocities of 300 m/s are sufficient to produce
353 phase scintillation without having much effect on the modeled signal intensity,
354 which is consistent with the observations.

355

356

357 **6. Acknowledgements**

358

359 We acknowledge the support of NSF Grant AGS-1311922 in performing this work
360 and NSF Grant PLR-1243398 in developing the SIGMA model. The EISCAT
361 experiment was led by PI Biagio Forte. Data can be retrieved from

362 <https://www.eiscat.se/madrigal/>. Scintillation data were collected by PI Cathryn
363 Mitchell on EPSRC grant EP/H003304/1 GNSS scintillation: detection, forecasting
364 and mitigation and can be obtained by contacting her.

365

366

367 **7. References**

368

369 Aarons, J. (1997), Global Positioning System phase fluctuations at auroral
370 latitudes, *J. Geophys. Res.*, **102**(A8), 17,219–17,231.

371

372 Aarons, J., Basu, S., 1994. Ionospheric amplitude and phase fluctuations at the GPS
373 frequencies. In: Proceedings of ION GPS-94, Arlington, VA, p. 1569.

374

375 Azeem, I., G. Crowley, A. Reynolds, J. Santana, and D. Hampton (2013), First results of
376 phase scintillation from a longitudinal chain of ASTRA's SM-211 GPS TEC and
377 scintillation receivers in Alaska, Proc. ION PNT.

378

379 Basu, S., MacKenzie, E., Basu, Su., 1988. Ionospheric constraints on VHF=UHF
380 communication links during solar maximum and minimum periods. *Radio Science*
381 **23**, 363.

382

383 Booker, H. G., J. A. Ratcliffe, and D. H. Shinn(1950), Diffraction from an irregular
384 screen with applications to ionospheric problems,*Philos. Trans. R. Soc.*
385 *London*, **242**(856),579–607.

386

387 Chisham, G., Lester, M., Milan, S. E., Freeman, M. P., Bristow, W. A., Grocott, A., ... &
388 Greenwald, R. A. (2007). A decade of the Super Dual Auroral Radar Network
389 (SuperDARN): Scientific achievements, new techniques and future
390 directions. *Surveys in Geophysics*, *28*(1), 33-109.

391

392 Costa, E., & Kelley, M. C. (1977). Ionospheric scintillation calculations based on in
393 situ irregularity spectra. *Radio Science*, *12*(5), 797-809.

394

395 Deshpande, K. B., Bust, G. S., Clauer, C. R., Rino, C. L., & Carrano, C. S. (2014). Satellite-
396 beacon Ionospheric-scintillation Global Model of the upper Atmosphere (SIGMA) I:
397 High-latitude sensitivity study of the model parameters. *Journal of Geophysical*
398 *Research: Space Physics*, *119*(5), 4026-4043.

399

400 Forte, B., & Radicella, S. M. (2004). Geometrical control of scintillation indices: what
401 happens for GPS satellites. *Radio science*, *39*(5).

402

403 Gola, M., A. W. Wernik, S. J. Franke, C. H. Liu, and K. C. Yeh. "Behaviour of HILAT
404 scintillation over Spitsbergen." *Journal of atmospheric and terrestrial physics* 54, no.
405 9 (1992): 1207-1213.

406

407 Kinrade, J., C. N. Mitchell, N. D. Smith, Y. Ebihara, A. T. Weatherwax, and G. S. Bust
408 (2013), GPS phase scintillation associated with optical auroral emissions: First
409 statistical results from the geographic South Pole, *J. Geophys. Res. Space Physics*,
410 118, 2490–2502, doi:10.1002/jgra.50214.

411

412 Kintner, P. M., Ledvina, B. M., & De Paula, E. R. (2007). GPS and ionospheric
413 scintillations. *Space Weather*, 5(9).

414

415 Knepp, D. L. (1983), Multiple phase-screen calculation of the temporal behavior of
416 stochastic waves, *Proc. IEEE*, 71(6), 722–737.

417

418 Prikryl, P., Jayachandran, P. T., Mushini, S. C., & Chadwick, R. (2011, February).
419 Climatology of GPS phase scintillation and HF radar backscatter for the high-latitude
420 ionosphere under solar minimum conditions. In *Annales Geophysicae* (Vol. 29, No. 2,
421 pp. 377-392). Copernicus GmbH.

422

423 Rino, C. L. (1979). A power law phase screen model for ionospheric scintillation: 1.
424 Weak scatter. *Radio Science*, 14(6), 1135-1145.

425

426 Skone, S., & De Jong, M. (2000). The impact of geomagnetic substorms on GPS
427 receiver performance. *Earth, Planets and Space*, 52(11), 1067-1071.

428

429 Skone, S., Knudsen, K., & De Jong, M. (2001). Limitations in GPS receiver tracking
430 performance under ionospheric scintillation conditions. *Physics and Chemistry of the*
431 *Earth, Part A: Solid Earth and Geodesy*, 26(6), 613-621.

432

433 Skone, S., F. Man, F. Ghafoori, R. Tiwari (2008), Investigation of scintillation
434 characteristics for high latitude phenomena, Proc. ION GNSS, 2425–2434, Savanna,
435 GA.

436

437 Smith, A. M., C. N. Mitchell, R. J. Watson, R. W. Meggs, P. M. Kintner, K. Kauristie, and
438 F. Honary (2008), GPS scintillation in the high arctic associated with an auroral arc.
439 *Space Weather*, 6(S03D01), ISSN:1542–7390.

440

441 Van Dierendonck, A. J., Klobuchar, J., & Hua, Q. (1993, September). Ionospheric
442 scintillation monitoring using commercial single frequency C/A code receivers. In
443 *proceedings of ION GPS* (Vol. 93, pp. 1333-1342).

444

445 Yeh, K. C., & Liu, C. H. (1982). Radio wave scintillations in the
446 ionosphere. *Proceedings of the IEEE*, 70(4), 324-360.

447